Analysis of a Rectangular Supersonic Multi-stream Jet by LES and Experiments

Matthew G. Berry

Dept. of Mechanical & Aerospace Engineering
Syracuse University
Syracuse, NY 13244
mgberry@syr.edu

Cory M. Stack

Dept. of Mechanical & Aerospace Engineering
The Ohio State University
Columbus, OH 43210
stack.49@osu.edu

Mohd Y. Ali

Dept. of Mechanical & Aerospace Engineering
Syracuse University
Syracuse, NY 13244
mali06@syr.edu

Andrew S. Magstadt

Dept. of Mechanical & Aerospace Engineering
Syracuse University
Syracuse, NY 13244
asmagsta@syr.edu

Datta V. Gaitonde

Dept. of Mechanical & Aerospace Engineering
The Ohio State University
Columbus, OH 43210
gaitonde.3@osu.edu

Mark N. Glauser

Dept. of Mechanical & Aerospace Engineering
Syracuse University
Syracuse, NY 13244
mglauser@syr.edu

ABSTRACT

This paper focuses on the analysis of a rectangular supersonic multi-stream jet with aft deck using large eddy simulation (LES) and experimental data. Proper orthogonal decomposition (POD) and Dynamic mode decomposition (DMD) are applied to time-resolved schlieren, stereo particle image velocimetry (PIV), and LES data. The spatial eigenfunctions of the two datasets reveal similar trends in the flow field, where structures with high mean squared value propagate from the nozzle lip and mixing layer. In the schlieren, acoustic waves can also be seen radiating from the nozzle lip and edge of the aft deck. By combining the spatial eigenfunctions from the schlieren experiment and the time-dependent snapshots of the LES, low-dimensional time characteristics for the flow are reconstructed. Additionally, we compare the spatial modes from the PIV and LES to determine how well the coherent structures are being captured in the simulation.

EXPERIMENTAL SETUP

The experiments presented herein were conducted in a $7.9m \times 6.1m \times 4.3m$ anechoic chamber, acoustically treated with fiberglass wedges to achieve a cut-off frequency of $\sim$150 Hz, seen in Figure 1. The facility houses an idealized three-stream nozzle with aft deck based on a variable-geometry engine cycle by Simmons (2009).

The engine design assumes a fully mixed fan flow far upstream of the nozzle's exit. In the context of this study, we view this as an idealized representation consisting of two canonical flows; a supersonic convergent-divergent (CD) jet and a sonic wall jet (representing the 3rd stream). The cross-sectional view of the nozzle can be seen in Figure 2. The main stream consists of a single expansion ramp nozzle (SERN), referred to as the bulk flow and containing the core and fan flow. The wall jet (3rd stream) is a convergent only variable bypass that enters the bulk flow in the CD nozzle's divergent section. The designed operating condition of the main jet is an ideally expanded $M_{j,1} = 1.6$. The 3rd stream is pulled from the bulk flow far upstream of the CD section and throttled using a set of butterfly valves. After passing through a convergent area, the bypass stream re-enters the main flow as a wall jet. Design condition for the 3rd stream is $M_{j,3} = 1.0$.

Figure 1: Anechoic chamber showing jet and microphone arrays with axes.

The jet is outfitted with a extended plate on one side of the nozzle's exit, representing an aircraft's aft deck. Additionally, the nozzle has the ability to rotate between runs, creating a hemispherical observation window around it. This gives the ability to observe the flow physics in different planes and acoustics above deck, below deck, and along the sideline of the jet. Dimensions and design conditions for the nozzle can be found in Magstadt *et al.* (2015).

The jet rig is operated by a 100 hp reciprocating Joy compressor. A 45 m^3 array of storage tanks create a blow-down facility capable of attaining supersonic jet speeds and a $Re \sim 2.7 \times 10^6$ for runs up to 1 minute.

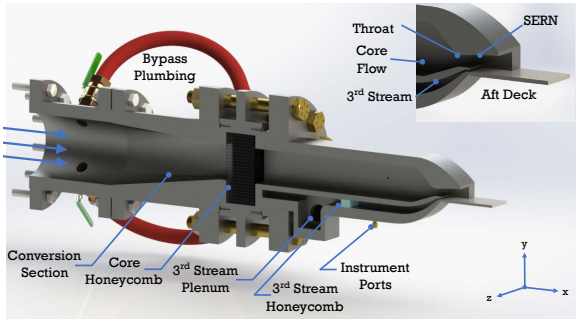

Figure 2: Cross sectional view of the idealized three-stream nozzle with aft deck installed at Syracuse University.

SCHLIEREN IMAGING

The schlieren utilizes optical inhomogeneities of refracted light rays to observe the flow. These light deviations show themselves as gradients proportional to the index of refraction, (n'). Illuminance corresponds to the first spatial derivative of the refractive index and directly relates to density gradients, in this case $\frac{\partial \rho}{\partial x}$. The schlieren system was arranged in a vertical z-type configuration, seen in Settles (2001) and Berry *et al.* (2016). The setup utilized twin 318 mm diameter parabolic mirrors with a 2.54 m focal length and a Luminus CBT-120 green LED pulsed light source modeled after Willert *et al.* (2012) and Wilson *et al.* (2015). A vertically oriented knife edge set at the second focal point operated at an 80% cutoff. Up to 2.5 million images were taken in each run with a Photron SA-Z high-speed camera sampling at two different rates. Due to the increased viewing area, the sampling rate for the largest window capped was 50 kHz. This window extends from the nozzle exit to $x/D_h \approx 6$ downstream. The camera exposure was set to 3.75×10^{-6} s.

PIV

Particle image velocimetry (PIV) was used to capture velocity vectors at several streamwise and cross-stream planes. This experiment incorporated a A NewWave Gemini Nd:YAG laser and two FlowSense EO 4MP cameras to resolved all 3 components of velocity. Seed particles were provided by a ViCount 1300 smoke generator. To avoid condensing water vapor in the flow, the nozzle was slightly heated to $\sim 170\ ^o$F. This brought the core flow above the atmospheric dew point. Images were captured at 10 Hz and 2400 snapshots were acquired per plane.

LES

For the LES, the full compressible Navier-Stokes equations are solved using the high-fidelity FDL3DI solver. In this simulation, the inviscid spatial fluxes are discretized using an upwind-biased, third-order Roe scheme with a Van Leer harmonic limiter. Viscous fluxes are discretized with second-order central differencing. Time integration is performed using an implicit second-order Beam-Warming scheme with two sub-iterations and approximate factorization, allowing for a time-step of approximately $\delta t \approx 47ns$. The full Reynolds number of the jet used $Re \approx 1.84 \times 10^6$ (based on major axis length), with no scaling. Previous results using this method on numerous jets are seen in Speth & Gaitonde (2013) and Gaitonde & Samimy (2011). For additional information regarding the scheme and formulation of FDL3DI, the reader is referred to Stack *et al.* (2016) and Gaitonde & Visbal (1998).

The nozzle exit conditions have been demonstrated to have a significant influence on the downstream evolution of the plume and its acoustic radiation characteristics (Bogey & Bailly (2010)). Ideally, the transition process of the interior nozzle boundary layers is included in the simulation, but the computational costs associated with the transition process are prohibitive for high Reynolds number flows. To avoid this costly computation, while simultaneously specifying realistic turbulent inflow conditions, a digital filtering method originally proposed by Klein *et al.* (2003), and later extended for compressible flows by Touber & Sandham (2008), is leveraged. This method has been further extended to allow the specification of turbulent profiles for two independent, rectangular streams for the geometry of this study. Additional details regarding the algorithm and initialization parameters can be found in Stack & Gaitonde (2017).

The single-block structured grid used in FDL3DI has dimensions of $1675 \times 705 \times 509$, corresponding to roughly 600M nodes. Around 65% of the grid points are before the end of the deck, as the grid is highly clustered in the streamwise direction near the upper nozzle lip and the deck edge. The grid was designed to account for the upward deflection of the plume as guided by experiments and preliminary simulations. The entire flow field was saved every 52 time steps (405kHz sampling rate), comprising a total of 4860 snapshots, corresponding to roughly 11.8 ms of physical time.

LOW-DIMENSIONAL MODELS

The temporal DMD algorithm used in the present work was adapted from Schmid (2010). The data set to be analyzed is a time-resolved schlieren snapshot record. A temporal sequence of N snapshots is ordered into column vectors ($\mathbf{v_j}$) that are equispaced in time. The primary basis of the method is that each snapshot in time, is connected to a subsequent snapshot, $\mathbf{v_{j+1}}$, by a linear mapping $\mathbf{A}$, such that, $\mathbf{v}_{j+1} = \mathbf{A}\,\mathbf{v}_j$. The eigenvalues and eigenvectors of the matrix $\mathbf{A}$ characterize the behavior of the dynamical system.

The assumption of constant mapping of the dynamical system, $\mathbf{A}$, between the snapshot sequence allows us to formulate a Krylov sequence of the data (Schmid (2010)). As the number of snapshots increase, the data set is assumed to approach a linear dependency. The last snapshot vector, $\mathbf{v}_N$, can be expressed as a linear combination of the previous linearly independent vectors,

$$\mathbf{v}_N = \mathbf{V}_1^{N-1}\,\mathbf{a} + \mathbf{r}, \tag{1}$$

where $\mathbf{r}$ is the residual vector and the coefficient $\mathbf{a}^T$ can be obtained using the least squares method.

Following Ruhe (1984), equation (1) can be written as follows in the matrix form:

$$\mathbf{A}\mathbf{V}_1^{N-1} = \mathbf{V}_2^N = \mathbf{V}_1^{N-1}\mathbf{S} + \mathbf{r}\,\mathbf{e}_{N-1}^T, \tag{2}$$

where $\mathbf{e}_{N-1}$ is the $(N-1)^{\text{th}}$ unit vector. The matrix $\mathbf{S}$ in (2) is of the companion type, which shifts the dataset (snapshot sequence) index from 1 to $N-1$. The number of snapshots, N, can be increased until the residual, $\mathbf{r}$, converges. The matrix $\mathbf{S}$ is a low-dimensional representation of the the full system matrix $\mathbf{A}$. The eigenvalues (λ_j) of matrix $\mathbf{S}$ approximate some of the eigenvalues of the full system matrix $\mathbf{A}$ (Schmid (2010)), and are also referred to as the Ritz values (Rowley *et al.* (2009)).

The companion matrix $\mathbf{S}$ is computed by calculating the singular value decomposition of the snapshot matrix $\mathbf{V}_1^{N-1}$ and the approximate 'full' matrix,

$$\tilde{\mathbf{S}} = \mathbf{U}^H\,\mathbf{V}_2^N\mathbf{W}\boldsymbol{\Sigma}^{-1} = \mathbf{U}^H\,\mathbf{A}\,\mathbf{U}, \tag{3}$$

which is obtained by projecting $\mathbf{A}$ on to $\mathbf{U}$. The matrix $\mathbf{U}$ contains the POD basis and forms the right singular vector of the snapshot

matrix $\mathbf{V}_1^{N-1}$. The eigenvalue decomposition of the matrix $\tilde{\mathbf{S}}$ gives the eigenvalues, λ_j, and eigenvectors, $\mathbf{y}_j$, such that $\tilde{\mathbf{S}}\mathbf{y}_j = \lambda_j \mathbf{y}_j$. Finally, the dynamic modes are computed as:

$$\mathbf{\Phi}_j = \mathbf{U}\mathbf{y}_j. \tag{4}$$

The approximate eigenvalues (Ritz values), λ_j, occur as complex conjugate pairs and lie on a unit circle in the complex domain Furthermore, the eigenvalues can be mapped logarithmically as, $\omega_j = \log(\lambda_j)/\Delta t$, where $\Delta t = f_s^{-1}$ is the separation time between successive snapshots. The discrete frequencies of the decomposed data, f_j, are determined from the imaginary part of the logarithmically mapped eigenvalues as $f_j = 2\pi\ \mathrm{Im}\{\omega_j\} = \arg(\lambda_j)/(2\pi\Delta t)$.

The negative frequencies are neglected and each mode pair is identified by the positive-valued frequency. The mean feature is a special case of DMD with zero eigenvalue (frequency), indicating that it is invariant in time. Beyond the zero-frequency case, the DMD modes can be sorted by their amplitudes, $||\mathbf{\Phi}||$.

Dynamic mode decomposition is closely related to the more commonly used POD modes. The POD modes can also be analyzed from the above discussed analysis. The singular value decomposition of matrix $\mathbf{V}_1^{N-1}$ contains the spatial structures ($\phi^n(\vec{x})$, the eigenvalues (diagonal matrix $\mathbf{\Sigma}$) according to which the POD modes are ranked, and the time-dependent coefficients ($a_n(t)$). In POD, spatial orthogonality of the identified structures is enforced, leading to multiple frequencies in each individual POD mode. A key difference between POD and DMD is that dynamic mode decomposition aims at an orthogonality in time by identifying pure frequencies.

POD was also used to analyze the experimental and LES datasets. This technique was first introduced into the turbulence community by Lumley (1967). POD has become a well-established method to find optimal basis functions by identifying the structures with largest mean square projection. Unlike Fourier analysis, where the data are decomposed into sines and cosines, POD determines the optimal basis functions by maximizing the mean square projection of the system using a spatial two-point correlation tensor in an eigenvalue problem.

The technique was later modified by Sirovich (1987) Sirovich (1987), who redefined the problem as a temporal formulation rather than a spatial one. This makes the calculations manageable for highly resolved spatial data, such as PIV or schlieren. The idea is to break down a spatiotemporal field into time-dependent coefficients and spatial basis functions. For the schlieren dataset, a scalar field is represented as the index of refraction, n'. The low-dimensional analysis on PIV data will use the streamwise component of velocity, u. A description of the POD process and derivation applied to a schlieren field can be seen in Berry *et al.* (2017).

BASELINE COMPARISONS

Baseline comparisons have already been made between experiments and LES in Stack & Gaitonde (2017). In the context of the schlieren, we will be using refractive index gradients from experimental data to perform the POD. For the LES, the streamwise density gradient field for the full three-dimensional flow was integrated across the span to mimic an experimental schlieren window.

Figure 3 shows the shock structures of both the experiment and simulation. Both images depict similar shock waves emanating from the top nozzle lip and from the nozzle's interior. Reflecting shocks bounce between the upper shear layer and aft deck until reaching the end of the deck plate.

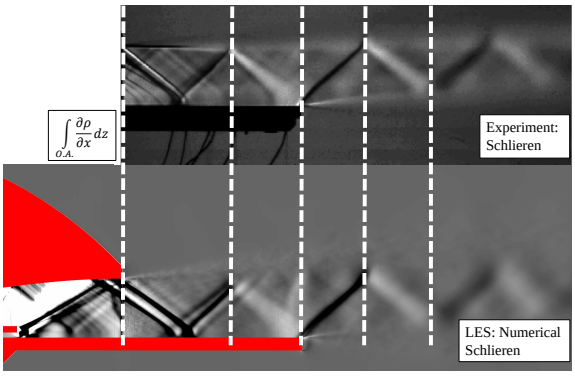

Figure 3: Comparison of time-averaged schlieren experiment and time-averaged LES numerical schlieren.

SCHLIEREN RESULTS

While the time support for the LES (405 kHz) can give time-dependent information of flow field, the ensemble is relatively small. Only 4860 time steps were collected from the integrated numerical schlieren, which were also spatially downsampled to the camera pixel locations, but giving very few statistically independent snapshots. Additionally, due to the complexity of the density fields and multitude of scales, the convergence rate of POD applied to schlieren data is extremely slow; seen in Berry *et al.* (2017). Because of these things, POD is unable to resolve most of the flow structures in the LES's numerical schlieren. However, if we assume similarities between the LES and experimental flows, we can use strengths from both to resolve time-dependent field information. We substitute the experimental POD eigenfunction, $\phi^{(n)}(\vec{x})$, as the spatial structure and the time-dependent LES field, $n'(\vec{x},t)$, as the schlieren snapshots. We can then reconstruct new time-dependent POD coefficients, $a_n(t)$, using equation 5 below, where N is the number of modes.

$$n'(\vec{x},t) = \sum_{n=1}^{N} a_n(t)\phi^{(n)}(\vec{x}) \tag{5}$$

Figure 4 shows the power spectral density (PSD) of the time-dependent POD coefficients for the schlieren (Figure 4a) and the reconstructed LES coefficients (Figure 4b). Previous schlieren experiments, near-field pressure sensors, far-field microphones, and LES results have showed this jet to have a dominant 34 kHz frequency propagating along the shocks through the entire flow field. This frequency is due to a Kelvin-Helmholtz instability at the intersection point between the main and bypass stream, as shown in Magstadt *et al.* (2016); Berry *et al.* (2017); Stack & Gaitonde (2017).

However, due to the decreased sampling rate of the larger schlieren window, the time-dependent information is aliased. With a sample rate of 50 kHz, Figure 4a shows the dominant 34 kHz K-H instability at 15.7 kHz. This is confirmed as the Nyquist frequency for this sample rate. After reconstructing $a_n(t)$ of the LES as described in equation 5, Figure 4b shows the 34 kHz signal is resolved. Similar trends are observed in the lower frequencies. A broadband peak around 3 kHz is evident in all of the modes except 1 and 2 as well as a broadband peak around 6.3 kHz in several modes. We can also notice broadband peaks at higher frequencies in the reconstructed data. Note that the spectra is noisier in the reconstructed data due to the small ensemble provided by the LES. Further, the amplitudes are different because the schlieren uses light intensity units arbitrarily scaled and the LES are units of streamwise density

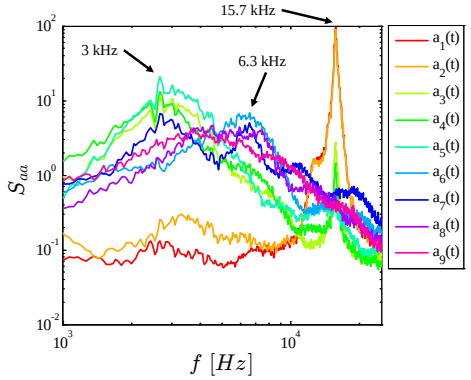

(a) Schlieren $a_n(t)$ spectra

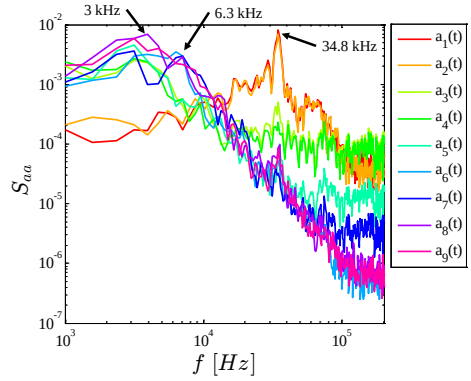

(b) Reconstructed LES $a_n(t)$ spectra

Figure 4: Power spectral density of $a_n(t)$).

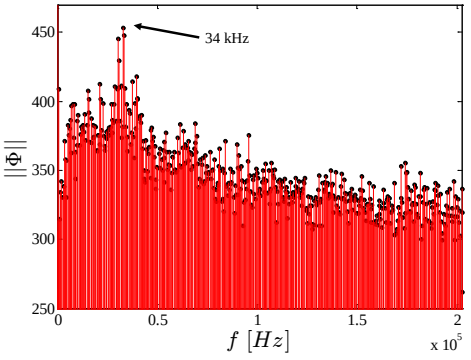

Figure 5: DMD Frequencies.

gradients.

Since the LES dataset is time-resolved, DMD can be leveraged to identify structures based on their growth rate and frequency. Figure 5 shows the peak frequencies extracted from the DMD analysis. This low-dimensional approach is able to identify the 34 kHz peak frequency. The DMD also shows a broad band peak around 7 kHz as well as sharp peaks at 15 kHz and 21 kHz.

Due to the sharp gradients of the numerical schlieren near the nozzle exit, the POD and DMD spatial modes are difficult to resolve. Figure 6 shows an instantaneous snapshot of the LES numerical schlieren. Since the data is well refined in the streamwise direction near nozzle lip, streamwise gradients can become very large relative to other locations where the grid is not as well resolved. This results in the "preference" of near lip gradient fluctuations. Thus we conclude, when attempting to apply low-dimensional models to pressure or density gradient fields, a Cartesian CFD grid or interpolating onto a Cartesian grid before computing the gradient would help resolve spatial modes.

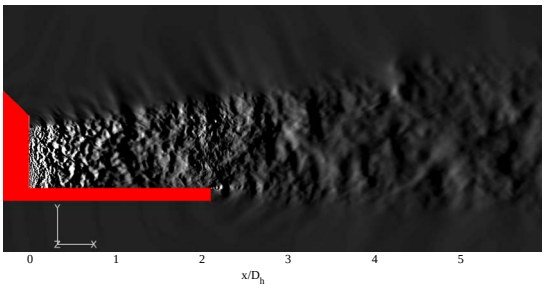

Figure 6: Instantaneous snapshot of LES numerical schlieren.

PIV RESULTS

Stereo PIV measurements were taken along the streamwise centerline plane and POD was performed on the velocity field dataset. This paper will only focus on the streamwise component of velocity. The viewing window begins at the nozzle exit plane and extends 4 hydraulic diameters downstream. Figure 7 shows the first 12 streamwise spatial eigenfunctions from the POD. Modes 1 and 2 show large scale structures beginning downstream of the aft deck edge in the top shear layer. As the mode number increases, smaller structures in the top shear layer can be seen farther upstream. Additionally, a large scale structure is seen in the bottom shear layer after the edge of the aft deck in modes 4, 6, 9, 10, and 12. Note that the boundary layer and a small section of the flow around the aft deck was masked out due to laser reflections that saturated the camera's CCD.

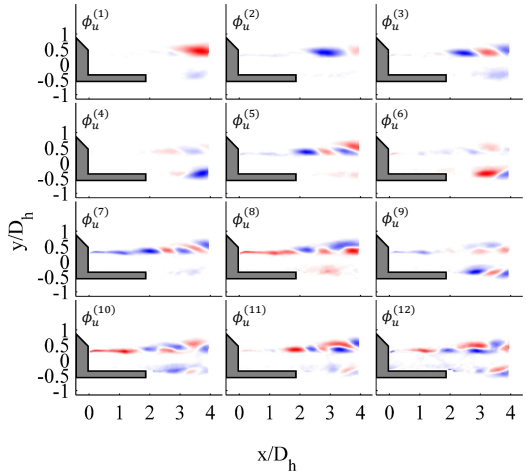

Figure 7: PIV Modes of u-component.

The same POD analysis was performed on the LES velocity field. Results from the LES were interpolated to match the respective PIV window. Figure 8 shows the first 12 spatial eigenfunctions for the POD. Several similarities are observed between the POD analyses. Modes 1 and 2 show similar large scale structures beginning downstream of the aft deck edge in the top shear layer. Once again, as the mode number increases, smaller structures in the top shear layer can be seen farther upstream. However, the LES is able

to identify a long thin flow structure along the aft deck, which is not seen is the PIV due to the laser reflections. It should also be noted that the 34 kHz did appear in some of the time-dependent POD coefficients, $a_u(t)$, but the spectral peak was fairly small.

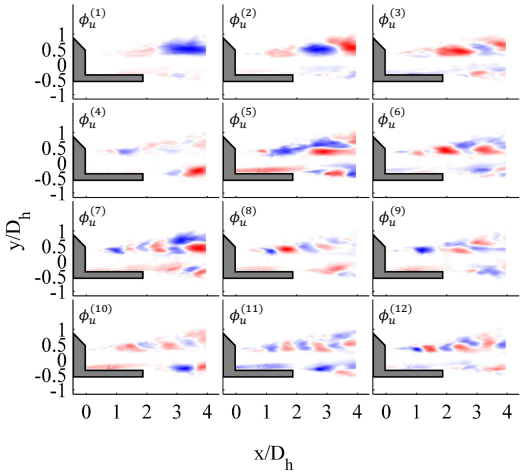

Figure 8: LES Modes of u-component.

Figure 9 shows the spatial correlation between each PIV and LES mode. The 4860 snapshots from the LES, despite lacking statistical independence, appear to resolve a few of the highest energy POD modes. Mode 1 has an 80% correlation between the experiment and simulation, while modes 2 and 3 have 60% correlation and mode 4 has 70% correlation. Additionally, mode 6 from the PIV has a 70% correlation to mode 10 of the LES. Since the streams were slightly heated to acquire PIV measurements, the nozzle temperature ratios (NTR) differ slightly. The LES and schlieren measurements were acquired at $NTR = 1.0$ and the PIV experiments were taken at $NTR \approx 1.2$ This may alter the spacing and placement of flow structures, thus affecting the spatial correlations. Additionally, masking out the PIV's laser reflection along the aft deck conceals structures in that region. A slightly heated case is currently being computed to match the temperatures of the LES and experiments.

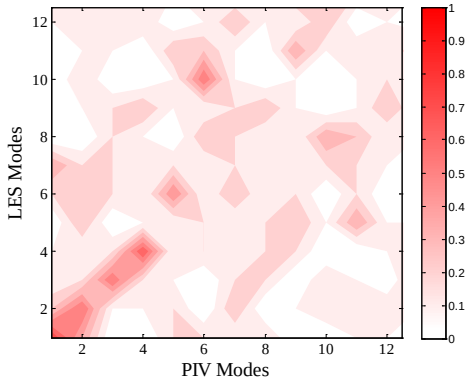

Figure 9: Spatial correlation between LES and PIV POD modes.

DMD analysis was also performed on the streamwise velocity of the LES. Figure 10a shows the peak frequencies. We can see that DMD was able to identify a dominant peak in the 34 kHz region.

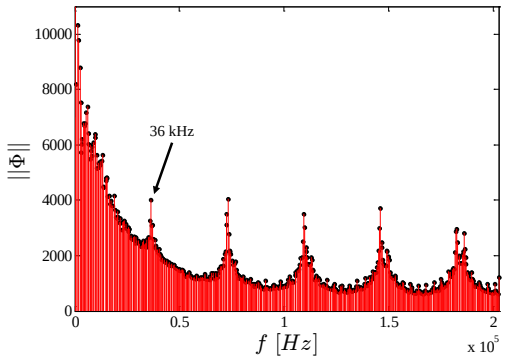

(a) DMD Frequencies of LES

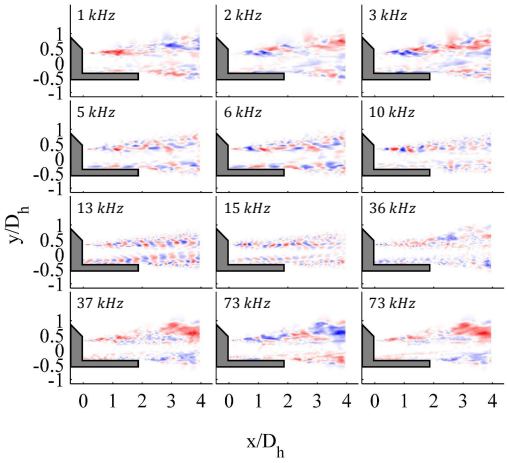

(b) DMD spatial structure

Figure 10: DMD of LES velocity field.

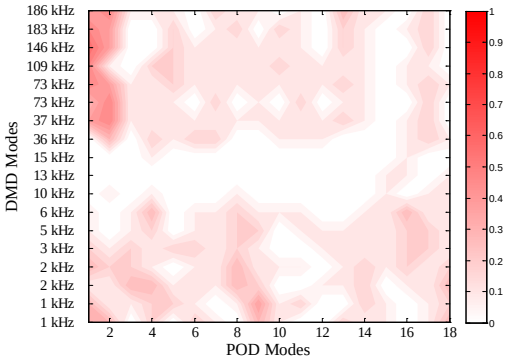

Figure 11: Spatial correlation between the DMD and POD modes of the LES velocity field.

Figure 10b shows the spatial modes for a few of the peak frequencies identified. The DMD is able to identify more coherent structures over the aft deck than the POD. The 5 kHz and 6 kHz modes distinctly show the mixing layer and top shear layer structures. The 13 kHz and 15 kHz modes identify the smaller scale structures in these regions as well as a distinction in structure size at the end of the aft deck. Small scale structures from entrainment can be seen as the bottom mixing layer becomes a free shear layer.

Figure 11 shows the spatial correlation between the DMD and POD modes of the LES velocity field. It is clear the mixing layer and shear layer structures between 10 kHz and 15 kHz modes of the DMD are not seen in the high energy POD modes. Additionally, the first two POD modes have strong correlations, between 40% and

60%, with the high frequency DMD modes. Further investigations are warranted, as these modes may be tied to the harmonics of the K-H instability.

CONCLUSION AND FUTURE WORK

A multi-stream SERN based on three-stream engines was analyzed both experimentally and through simulations. Time-resolved schlieren measurements and PIV were compared to LES. Baseline analysis between the LES numerical schlieren and experimental schlieren showed similar shock characteristics and flow structures. Both the LES's numerical schlieren and experiments identified a K-H instability propagating through the flow that emanates from the intersection of the main and bypass stream. Performing POD on the largest schlieren window, sampled at 50 kHz, aliased the 34 kHz K-H structure to 15.7 kHz. However, due to the 405 kHz sampling rate of the LES, the 34 kHz can be resolved. By projecting the spatial eigenfunctions of the experiment onto the LES snapshots, new reconstructed time-dependent POD coefficients were calculated. The PSD of these POD coefficients identify the 34 kHz previously aliased in the experiment as well as other lower frequency peaks. Performing DMD on the LES dataset was also able to identify a similar peak at 34 kHz associated with the K-H instability. However, the small ensemble from the simulation prevented a convergence of the spatial modes and makes it difficult to identify these 34 kHz structures in the LES.

POD analysis was also performed on experimental and simulated velocity data. Due to the faster convergence of velocity modes compared to schlieren, POD was able to resolve the first few high energy modes from the LES data. The spatial eigenfunctions were correlated to the PIV modes and identified a relationship between the first 4 modes correlating up to 80%. However, because the PIV was heated to reduce condensation in the jet, the flow structures may differ slightly from the LES. A new LES dataset is currently being run to match temperatures between LES and PIV.

DMD analysis was applied to the LES velocity data. The high frequency peak at $\sim$34 kHz was dominant in the DMD amplitude, but was only faintly seen in the POD analysis. Structures in the mixing layer and shear layers were identified between 10 kHz and 15 kHz that were not seen the the first several POD modes. Additionally, more flow structures were identified over the aft deck than were seen in the high energy POD modes. This shows how DMD and POD highlight different characteristics of the velocity field for this particular jet. More work is being complete to change observation windows as well as increasing the LES ensembles.

ACKNOWLEDGMENTS

The authors would like to acknowledge AFOSR, program manager Dr. Doug Smith, for funding this research, Grant No. FA9550-15-1-0435. The authors would also like to acknowledge Spectral Energies, LLC. Phase II SBIR, with Dr. Alex Giese, Thomas Ferrill, and AFRL for the ongoing support and interactions throughout these research endeavors. Additionally, the authors acknowledge Dr. Jacques Lewalle, Pingqing Kan, Andrew Tenney (Syracuse University), and Dr. Barry Kiel (AFRL) for many insightful discussions throughout the experiments and analysis. Finally, thanks to Dr. James Gord, Amy Lynch, and Dr. Benjamin Halls for providing valuable equipment and Thomas Coleman (Syracuse University) for helping to acquire this comprehensive dataset.

REFERENCES

Berry, M. G., Magstadt, A. S. & Glauser, M. N. 2017 Application of pod on time-resolved schlieren in supersonic multi-stream rectangular jets. *Physical of Fluids* **29** (Iss. 2).

Berry, Matthew G., Magstadt, Andrew S., Glauser, Mark N., Ruscher, Christopher J., Gogineni, Sivaram P. & Kiel, Barry V. 2016 An acoustic investigation of a supersonic, multi-stream jet with aft deck: Characterization and acoustically-optimal operating conditions. 54^{th} *AIAA ASM* .

Bogey, C. & Bailly, C. 2010 Influence of nozzle-exit boundary-layer conditions on the flow and acoustic fields of initially laminar jets. *Journal of Fluid Mechanics* **663**, 507–538.

Gaitonde, D. & Samimy, M. 2011 Coherent structures in plasma-actuator controlled supersonic jets: Axisymmetric and mixed azimuthal modes. *Physics of Fluids* **23** (9).

Gaitonde, D. & Visbal, M. 1998 High-order schemes for navier-stokes equations: Algorithm and implementation into fdl3di. Tech. Rep. AFRL-VA-WP-TR-1998-3060. Air Force Research Laboratory, Wright-Patterson AFB.

Klein, M., Sadiki, A. & Janicka, J. 2003 A digital filter based generation of inflow data for spatially developing direct numerical or large eddy simulations. *Journal of Computational Physics* **186** (2), 652–665.

Lumley, J. L. 1967 The structure of inhomogeneous turbulent flows. *Atm. Turb. and Radio Wave Prop. ed. by A.M. Yaglom and V. I. Tatarsky, (Nauka, Moscow)* pp. 166–178.

Magstadt, A.S., Berry, M.G., Shea, P.R., Glauser, M.N., Ruscher, C.J., Gogineni, S.P. & Kiel, B.V. 2015 Aeroacoustic experiments on supersonic multi-aperture nozzles. In *51^{st}AIAA Joint Propulsion Conference*. Orlando, FL.

Magstadt, Andrew S., Berry, Matthew G., Coleman, Thomas J., Shea, Patrick R., Glauser, Mark N., Ruscher, Christopher J., Gogineni, Sivaram P. & Kiel, Barry V. 2016 A near-field investigation of a supersonic, multi-stream jet: locating turbulence mechanisms through velocity and density measurements. *51^{st}AIAA Aerospace Sciences Meeting* .

Rowley, Clarence W., Mezić, Igor, Bagheri, Shervin, Schlatter, Philipp & Henningson, Dan S. 2009 Spectral analysis of nonlinear flows. *Journal of Fluid Mechanics* **641**, 115–127.

Ruhe, Axel 1984 Rational krylov sequence methods for eigenvalue computation. *Linear Algebra and Appl.* **58**, 391–405.

Schmid, Peter J. 2010 Dynamic mode decomposition of numerical and experimental data. *Journal of Fluid Mechanics* **656**, 5–28.

Settles, G.S. 2001 *Schlieren & Shadowgraph Techniques*. Springer.

Simmons, Ronald J. 2009 Design and control of a variable geometry turbofan with an independently modulated third stream. PhD thesis, The Ohio State University.

Sirovich, L. 1987 Turbulence and the dynamics of coherent structures, part i,ii, and iii. *Quarterly Applied Mathematics* **45**.

Speth, R. & Gaitonde, D. 2013 Parametric study of a mach 1.3 cold jet excited by the flapping mode using plasma actuators. *Computers and Fluids* **84**, 16–34.

Stack, Cory M. & Gaitonde, Datta V. 2017 Dynamical features of a supersonic multistream nozzle with an aft-deck. 54^{th} *AIAA ASM* (AIAA 2017-0557).

Stack, C. M., Gaitonde, D. V., Agostini, L., Berry, M. G., Magstadt, A. S. & N., Glauser M. 2016 Numerical investigations of a supersonic multistream jet with an aft-deck. 54^{th} *AIAA ASM* .

Touber, E. & Sandham, N. D. 2008 Oblique shock impinging on a turbulent boundary layer: Low-frequency mechanisms. 38^{th} *Fluid Dynamics Conference and Exhibit* (AIAA 2008-4170).

Willert, C. E., Mitchell, D. M. & Soria, J. 2012 An assessment of high-power light-emitting diodes for high frame rate schlieren imaging. *Experiments in Fluid* **53** (2), 413–421.

Wilson, S., Gustafson, G., Lincoln, G., Murari, K. & Johansen, C. 2015 Performance evaluation of an overdriven led for high-speed schlieren imaging. *Journal of Visualization* **18** (1), 35–45.